Controlling the Nucleation of a Semicrystalline Polymer by Inducing Compartmentalization of Competitive Nucleating Agents

Arnaud Y.-g. Delplanque, Sandra Casale, Bruno Bresson, Paolo Edera, Clément Guibert, Nathan J van Zee

RESEARCH ARTICLE

NANO · MICRO small
www.small-journal.com

Controlling the Nucleation of a Semicrystalline Polymer by Inducing Compartmentalization of Competitive Nucleating Agents

*Arnaud Y.-G. Delplanque, Sandra Casale, Bruno Bresson, Paolo Edera, Clément Guibert, and Nathan J. Van Zee**

Many functional polymeric systems have been inspired by the principle of compartmentalization, a ubiquitous form of hierarchical assembly found in Nature. For instance, polymers have been elaborated with microcapsules that release a chemical payload upon activation by an external stimulus. A fascinating challenge it to design a polymeric system to perform the opposite function, i.e., to load a cargo into a dispersed minor phase. Herein, this concept is exemplified in the context of a semicrystalline polymer matrix that contains two nucleating agents, one based on a supramolecular assembly and another based on a covalent triblock copolymer. These two additives compete to nucleate the semicrystalline matrix according to their competitive nucleation efficiency. A functional copolymer is rationally designed to induce these two additives to spatially assemble together. By adding a small amount of the functional copolymer, the supramolecular assembly remarkably segregates to the block copolymer phase, which profoundly impacts the interface between the block copolymer phase and the matrix. The compartmentalized additives no longer exhibit nucleating properties for the matrix, and the resulting material shows essentially the same thermomechanical properties as the virgin matrix.

1. Introduction

Compartmentalization is a ubiquitous form of hierarchical assembly[1] found in Nature, where chemical processes are spatially segregated.[2] One intriguing example is bacterial microcompartments, which are composed of an enzyme core that is encapsulated by a functional protein shell.[3] Compartmentalization permits control over the local concentration of intermediates, minimizes competition with other metabolic pathways, and enhances the stability of the enzyme core. This concept is essential to the function of natural biological systems, and it has served as the inspiration for the design of synthetic biomaterials, such as supramolecular tissue scaffolds, functional polymer nanoparticles, and artificial organelles and cells.[4–11]

The utility of compartmentalization is not limited to life-like systems under physiological conditions. It has inspired the design of functional bulk materials as well, enabling useful properties such as self-reparability, damage reporting, shape memory, and controlled release of chemical payloads.[12–15] In the particular case of semicrystalline polymers, the most widely produced class of polymers today,[16] the concept of compartmentalization has been elegantly utilized to address a persistent challenge in material science—the rational control of polymer nucleation. Many polymers in commercial products are nucleated by impurities that have accumulated from their synthesis and processing. An effective strategy to unravel the complex nucleating properties of these species is to compartmentalize a semicrystalline polymer as droplets in an immiscible polymer matrix.[17,18] The impurities are distributed throughout the matrix and the droplet phase; when the number of droplets is on the same order of magnitude as the number of impurities, the material undergoes fractionated crystallization, where populations of droplets are each nucleated by a different kind of heterogeneity. This approach allows for other competing processes to be elucidated, such as homogeneous and surface nucleation, in amorphous and semicrystalline matrices.[19,20]

Some commercial semicrystalline polymers, notably isotactic polypropylene (*i*PP), exhibit relatively slow crystal growth

A. Y.-G. Delplanque, P. Edera, N. J. Van Zee
Chimie Moléculaire, Macromoléculaire, Matériaux, ESPCI Paris, CNRS
Université PSL
Paris 75005, France
E-mail: nathan.van-zee@espci.psl.eu

S. Casale, C. Guibert
Laboratoire de Réactivité de Surface, UMR 7197, CNRS
Sorbonne Université
Paris F-75005, France

B. Bresson
Laboratoire de Sciences et Ingénierie de la Matière Molle, ESPCI Paris, CNRS
PSL University
Paris 75005, France

The ORCID identification number(s) for the author(s) of this article can be found under https://doi.org/10.1002/smll.202507875

DOI: 10.1002/smll.202507875

kinetics, which slows processing times and thus necessitates the use of additives to increase the density of nuclei.[21,22] The choice of such additives, commonly known as nucleating agents, remains largely based on empirical studies.[23] Nucleating agents are dispersed throughout the polymer matrix in the molten state, and they typically have nanoscale features that promote the nascent organization of polymer chains into a nucleus. Recently, such nucleating agents have also been compartmentalized within incompatible polymer phases to control their spatial distribution within the material. Several groups[24–29] have used polyamide particles and fibers to modulate the dispersion of a dicarboxamide nucleating agent in *i*PP. The polyamide was preloaded with the nucleating agent and then dispersed in the *i*PP at relatively low temperature; upon heating above the melting temperature of all components, the dicarboxamide leached from the polyamide phase, assembled into needle-like crystals, and locally nucleated the *i*PP matrix. This strategy has been shown to enhance the mechanical properties of *i*PP/polyamide blends.

In this context, we were fascinated by the fundamental challenge of compartmentalizing multiple nucleating agents within a polymer matrix in the molten state. Compared to previous work, such a system entails gathering a cargo (as opposed to releasing it), and we sought to exemplify this concept where the number of compartments is much less than the quantity of nucleating sites. In addition to addressing fundamental questions of hierarchical assembly, we believe that this challenge has important implications for mechanical recycling,[30] additive manufacturing,[31] and supramolecular enhancement of polymers and networks.[32–37]

As a proof-of-concept, we designed a model system based on *i*PP in which two orthogonal nucleating agents, one based on a supramolecular assembly and another based on a covalent triblock copolymer, were compartmentalized by employing a functional copolymer. A commercial grade of *i*PP (identified as **PP**) was chosen as the matrix because its hierarchical structure can be easily characterized and is highly sensitive to the presence of nucleating agents.[21,23,38,39] For the supramolecular assembly-based nucleating agent, inspired by the previous work of Smith and Schmidt,[40–43] we chose the trialkyl benzene-1,3,5-tricarboxamide **BTA** (**Figure 1A**, left), which exclusively nucleates the α-form of *i*PP. **BTA** dissolves in molten *i*PP at high temperature and self-assembles upon cooling via hydrogen bonding and π–π interactions to form needle-like structures.[43] These assemblies promote epitaxial crystallization of *i*PP on their surface,[44] increasing the crystallization temperature and influencing the morphology of the crystalline domains (Figure 1A). Regarding the covalent block copolymer-based nucleating agent, the triblock copolymer polystyrene-*block*-poly(ethylene-*co*-1-butene)-*block*-polystyrene (PS-*block*-PEB-*block*-PS or **SEBS**, Figure 1B, left) was selected. At high temperature, **SEBS** forms phase-separated droplets dispersed in *i*PP. Cooling below its order-disorder transition temperature induces its self-organization into a lamellar structure.[45,46] **SEBS** acts as a nucleating agent for *i*PP through the interplay of the *i*PP-compatible PEB lamellae and the rigidity of the *i*PP-incompatible polystyrene domains (Figure 1B).[47,48]

We designed a functional copolymer to act as a compartmentalization agent by incorporating structural motifs that favorably interact with both the supramolecular assembly and the covalent block copolymer. This design was predicted to induce **SEBS** and **BTA** to assemble in the same regions in the material. The compatibilization agent, identified as **gSEBS** (Figure 1C, middle), is composed of the **SEBS** backbone in which the PEB block is selectively grafted with pendant benzene tricarboxamide (**BTA**) units substituted with two tert-octyl groups. From a previous study, we found that similar structures favorably coassemble with **BTA**.[49,50]

A series of increasingly complex compositions were prepared and comprehensively studied from the nano- to the macroscale. In the absence of the compartmentalization agent, **SEBS** and **BTA** formed self-sorted assemblies and competed to nucleate **PP**. Upon adding a small amount of **gSEBS**, **BTA** assemblies were sequestered within the block copolymer phase, thereby suppressing the nucleating capacity of both additives. The resulting materials exhibited properties analogous to those of virgin **PP**, thereby exemplifying the effective compartmentalization of the additives.

2. Results and Discussion

2.1. Preparation of the Components and Sample Preparation

The isotactic polypropylene used for this study (**PP**) was a commercial homopolymer with an average molar mass (M_n) of 42 kg mol^{-1} and a dispersity ($Đ$) of 6.1. Certain control compositions were prepared with a commercial grade of polystyrene (designated as **PS**) with a weight-average molar mass of 192 kg mol^{-1}. **BTA** was synthesized in one step according to a literature procedure.[42] A commercial PS-*block*-polybutadiene-*block*-PS (SBS) symmetric triblock copolymer was hydrogenated to produce **SEBS** with an M_n of 27.2 kg mol^{-1} and a $Đ$ of 1.04. The total molar styrene content was 34% (i.e., each PS end-block is composed of 17 mol.%). The PEB midblock was composed of 93 mol.% of 1-butene units, which renders it amorphous but compatible with the amorphous domains of *i*PP.[51] The relatively low molar mass of this copolymer enables fast diffusion in polymer melts.[52]

Finally, the compatibilization agent **gSEBS** was synthesized by post-polymerization modification and functionalization of the same commercial SBS used to make **SEBS**, notably via thiol-ene grafting and amide coupling. The synthesis is detailed in the Supporting Information. An average functionalization of 5 BTAs per chain was selected to achieve a balance between a sufficiently low local BTA concentration to ensure complete supramolecular dissociation at processing temperatures and a high enough degree of grafting to minimize the amount of **gSEBS** required to reach the targeted global concentration.

Compositions ranging from binary to quaternary blends (Table S1, Supporting Information) were prepared using a solvent-free protocol with a micro-compounder. To provide a basis of comparison, a series of blends of **BTA** in different matrices were formulated involving **PP** and/or **PS**, which constitute two of the blocks of **SEBS** (**PP/BTA**, **PS/BTA**, and **PP/PS/BTA**). The volume ratio of **PS** to **PP** in **PP/PS/BTA** was set to 7%, which is the volume ratio of PS to **PP**+PEB in the subsequent triblock-containing compositions. For these samples as well as all subsequent ones (unless specified otherwise), the total weight concentration of BTA units was kept at 9.2 µmol per gram of material. To characterize the triblock behavior and its interactions with the matrix, the binary blend **PP/SEBS** was prepared. The orthogonality of the assembly of **BTA** and **SEBS** was

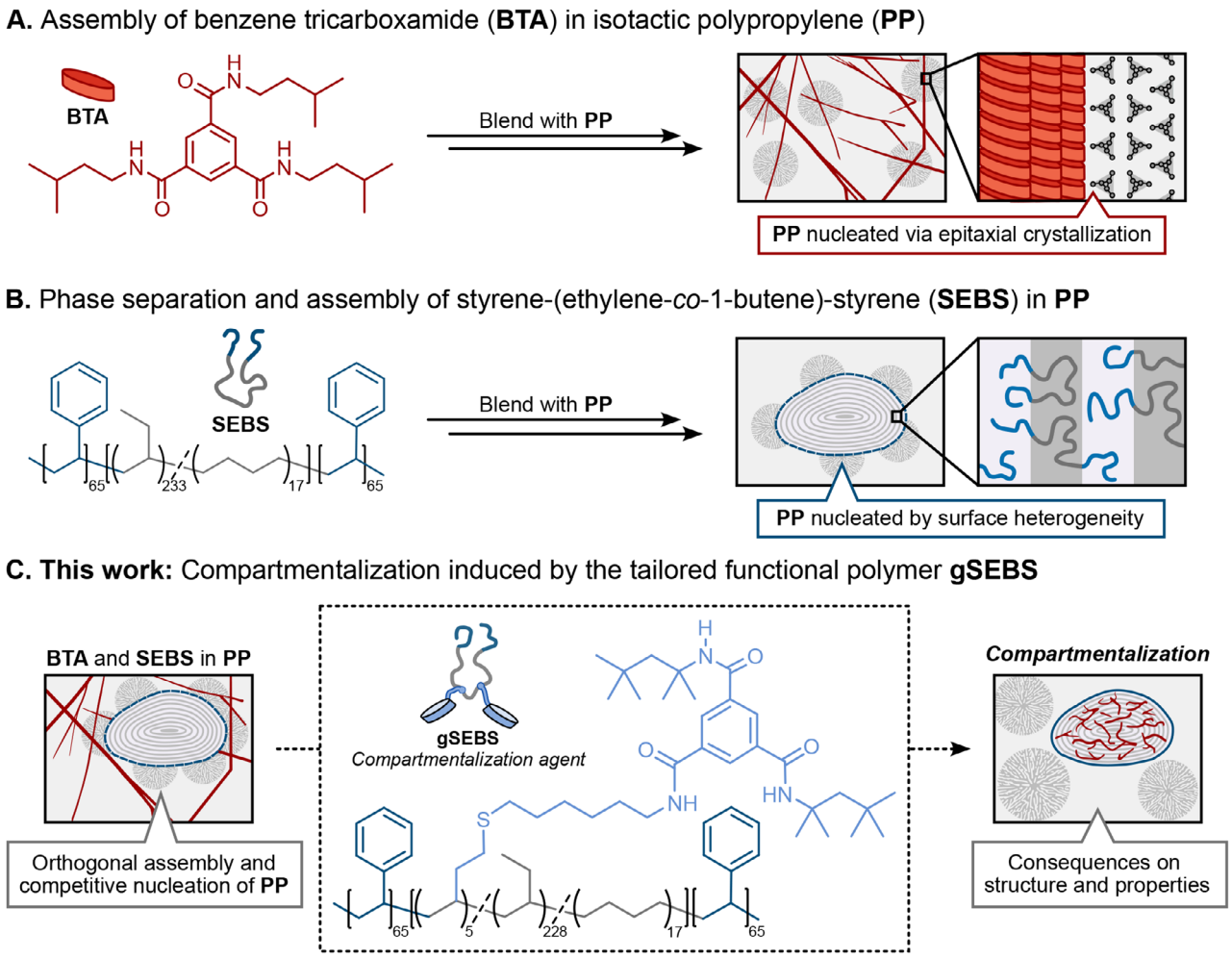

Figure 1. A) Assembly of the benzene tricarboxamide (**BTA**) into a supramolecular aggregate that nucleates isotactic polypropylene (**PP**) via epitaxial crystallization. B) Assembly of the polystyrene-*block*-poly(ethylene-*co*-1-butene)-*block*-polystyrene triblock copolymer (**SEBS**) into phase-separated domains that nucleate **PP** through surface heterogeneities. C) Compartmentalization of the **BTA** and **SEBS** by incorporating the functional polymer **gSEBS**.

assessed in the tertiary blend **PP/SEBS/BTA**. Finally, the impact of the compartmentalization agent **gSEBS** was elucidated with the tertiary blend **PP/SEBS/gSEBS** and the quaternary blend **PP/SEBS/gSEBS/BTA**.

2.2. BTA and SEBS Homoassembly and Nucleating Properties

The key results from the study of **BTA** and **SEBS** homoassemblies and their corresponding nucleating properties are described in this section. Extended data and discussion concerning the spectroscopic analysis, morphology, and nucleating properties of **BTA** assemblies, as well as the self-organization of **SEBS** in the bulk and in **PP**, are provided in the Supporting Information.

*2.2.1. Homoassembly of **BTA** in **PP**, **PS**, and **PP/PS***

The homoassembly of **BTA** (**Figure 2A**) in **PP/BTA**, **PS/BTA**, and **PP/PS/BTA** was studied by variable-temperature Fourier-transform infrared (FTIR) spectroscopy upon cooling and then heating between 260 and 170 °C. In each of the matrices, **BTA** assembled by a nucleation-elongation mechanism as evidenced by the non-sigmoidal shape of the heating and cooling curves (Figures 2B,C; S1, Supporting Information).[53] The elongation temperatures on cooling ($T_{e,BTA}'$, Figure 2B) were estimated using a tangent line method, while the elongation temperatures on heating ($T_{e,BTA}$, Figure 2C) were calculated using the nucleation-elongation mass-balance model of ten Eikelder and Markvoort (Table S2, Supporting Information).[54] The variations in $T_{e,BTA}$ can be attributed to the stabilization of **BTA** in its monomeric form by the aromatic **PS** matrix.

Imaging of **PP/PS/BTA** by polarized optical microscopy (POM) allowed for the direct visualization of the assembly process, which appeared as a single continuous event yielding bundles of fibers with a length of hundreds of micrometers (**Figures 3A**; S2B, Supporting Information). The needle-like **BTA** assemblies and the spherical domains of **PS** are also clearly visible in the **PP** matrix by scanning electron microscopy (SEM) after cryo-fracture of the sample (Figure 3B).

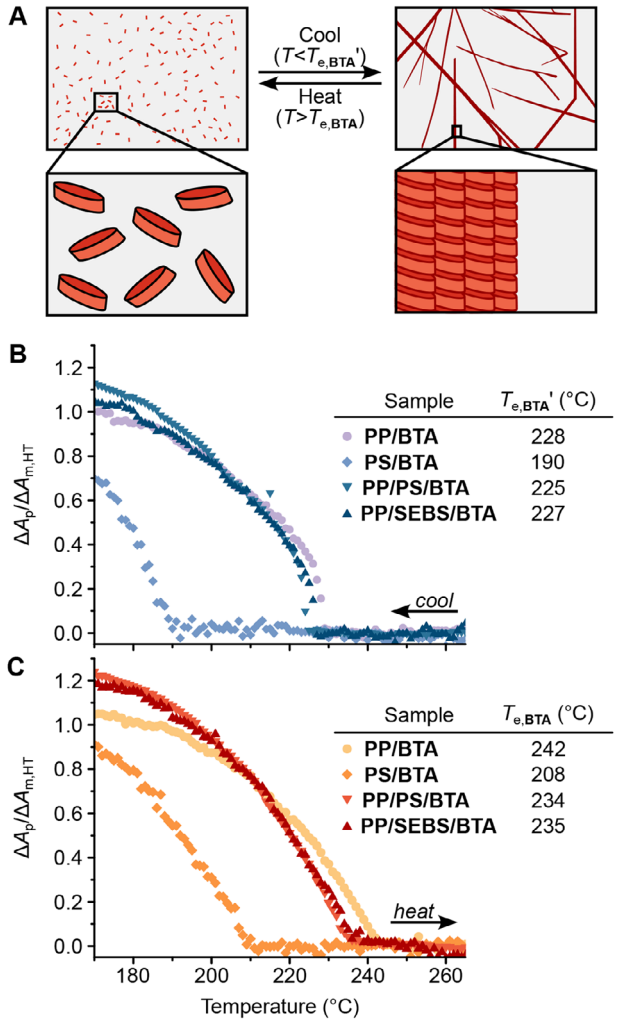

Figure 2. A) Schematic representation for the assembly and disassembly of **BTA**s. Fourier-transform infrared (FTIR) spectroscopy cooling B) and heating C) curves of **BTA** assembly in **PS/BTA**, in **PP/BTA**, in **PP/PS/BTA**, and in **PP/SEBS/BTA** at a concentration of 9.2 µmol g^{-1} of material at a rate of ± 1 °C min^{-1}. Tabulated values for the elongation temperatures measured upon heating and cooling ($T_{e,BTA}$, and $T_{e,BTA}$', respectively) are provided in the respective legends.

Differential scanning calorimetry (DSC) experiments were performed to characterize the thermal behavior of the **PP** matrix (Figure S3 and Table S3, Supporting Information), as it reveals crystallization and melting transitions and enables comparative evaluation of the nucleation efficiency through analysis of crystallization peak temperatures. For example, the peak crystallization temperature of **PP** ($T_{c,PP}$) detected for **PP/PS/BTA** was increased by 5 °C compared to that of **PP/PS**, demonstrating the nucleating properties of the assembled **BTA**.

2.2.2. Homoassembly of *SEBS* in *PP/SEBS* Blend

When dispersed in **PP**, the **SEBS** phase of **PP/SEBS** exhibited similar properties as in the bulk (Supporting Information). Small-angle X-ray scattering (SAXS) measurements performed at room temperature on **PP/SEBS** enabled the identification of the same intense peak assigned to the **SEBS** lamellae in the bulk material with a marginal shift in $q_{L,max}$ to 4.93 × 10^{-2} $Å^{-1}$, which corresponds to a long period of 12.7 nm (**Figure** 4A). By variable-temperature SAXS, this peak appeared below an order–disorder transition temperature ($T_{ODT,SEBS}$) of 166 °C (Figure 4B). The proximity of this value to that observed in the bulk supports the assertions that the triblock forms its own dispersed phase and that its morphology is retained when blended in **PP** (Figures S4 and S5, Supporting Information).

These conclusions are corroborated by direct observations using optical and electron microscopy. Upon cooling to 165 °C, the **SEBS** domains exhibited birefringence, manifesting as Maltese crosses (Figures 3C; S6B, Supporting Information). This phenomenon is indicative of alignment in ordered concentric lamellar structures, in agreement with the features observed by SAXS.[55] This organization was also confirmed by transmission electron microscopy (TEM) imaging (Figure 3D, right), which appeared as darkly stained PS domains and relatively lightly stained PEB lamellae. The mean long period was measured to be 12.5 nm, in line with the measurement by SAXS.

Based on DSC, the $T_{c,PP}$ detected for **PP/SEBS** was 130 °C, which is 8 °C higher than that observed for pristine **PP** (Figure S7 and Table S3, Supporting Information). The nucleating properties for triblock copolymers like **SEBS** have been previously explained by the interpenetration of *i*PP chains in the PEB lamellae at the interface of the triblock copolymer phase; the rigid PS domains are proposed to act as heteronuclei.[47,48] This behavior is strikingly evident in the present system. At the interface of **PP** and **SEBS**, the lamellae appear to become exfoliated from the swelling of the PEB domains of **SEBS** by **PP** (Figure 3D, left). The darkly stained PS domains of **SEBS** thus create a rough surface texture.

2.3. Orthogonal Assembly and Competitive Nucleation in PP/SEBS/BTA

2.3.1. Elucidation of Orthogonal Assembly

The assembly of **BTA** in the ternary blend **PP/SEBS/BTA** was elucidated by FTIR spectroscopy and displayed a similar evolution as in **PP/PS/BTA**. Indeed, the cooling and heating curves essentially overlap between these two samples, and the fitted $T_{e,BTA}$ values for **PP/SEBS/BTA** and **PP/PS/BTA** are nearly the same (235 and 234 °C, respectively; Figure 2C; Table S2, Supporting Information). Given that the concentration of **BTA** and the volume ratio of PS to **PP**+PEB were identical in both compositions, the similarity observed by FTIR spectroscopy indicates that the triblock copolymer did not disrupt the assembly of **BTA**. Direct observations by POM support this conclusion, as structures of the same size and needle-like morphology appear in both blends at the same temperature upon cooling (Figures 3E; S8B, Supporting Information). SEM imaging confirms the similarity of **BTA** assemblies between **PP/PS/BTA** and **PP/SEBS/BTA** and facilitates the elucidation of their spatial distribution: the **BTA** structures are uniformly dispersed in the sample both in the **PP** and the **SEBS** phase and across interfaces (Figures 3F; S9, Supporting Information).

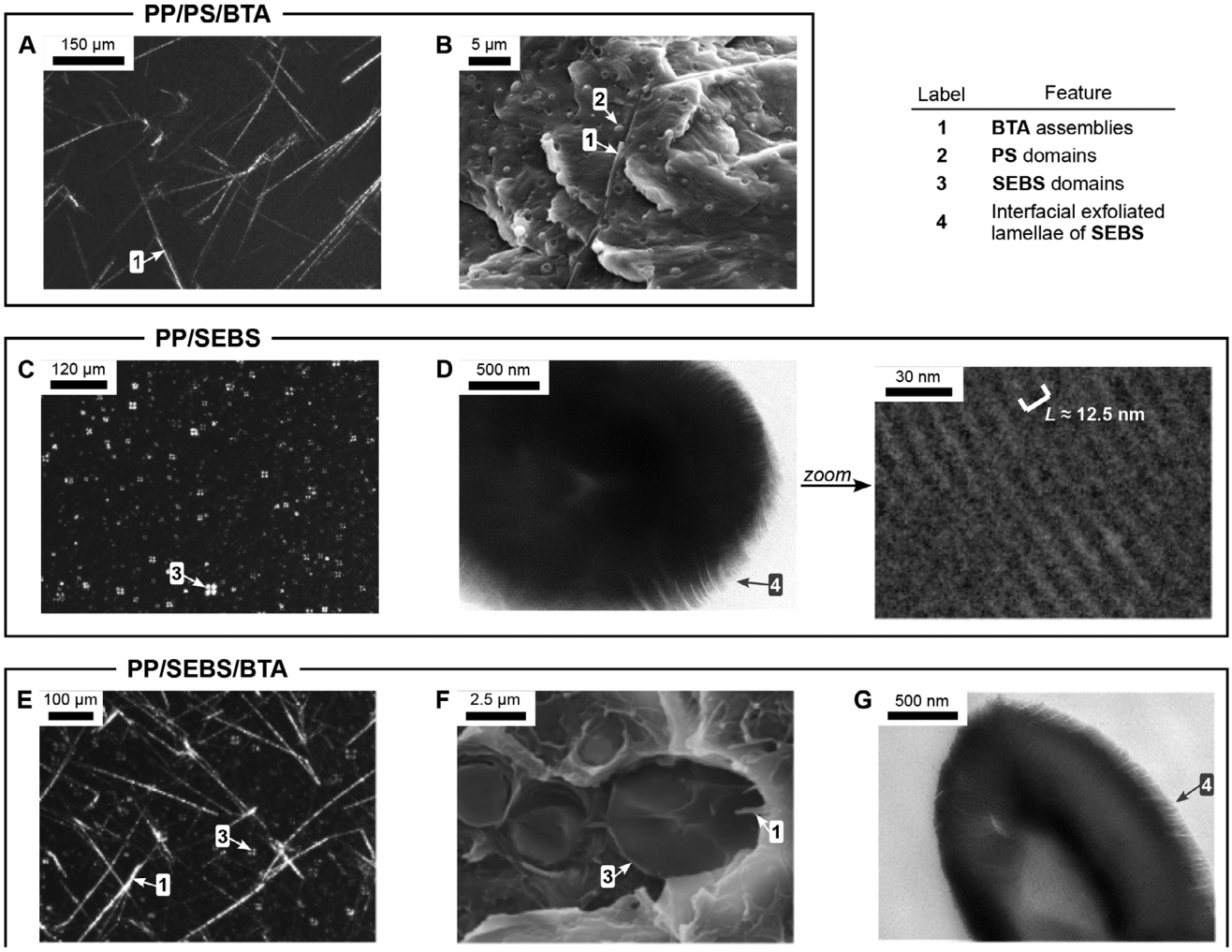

Figure 3. A) Polarized optical microscopy (POM) image of **PP/PS/BTA** at 158 °C. B) Scanning electron microscopy (SEM) image of **PP/PS/BTA**. C) POM image of **PP/SEBS** at 165 °C. D) Transmission electron microscopy (TEM) images of the **PP–SEBS** interface in **PP/SEBS** (left), along with a zoomed view of the lamellae (right). E) POM image of **PP/SEBS/BTA** at 163 °C. F) SEM image of **PP/SEBS/BTA**. G) TEM image of the **PP–SEBS** interface in **PP/SEBS/BTA**. POM images were acquired while cooling at −1 °C min^{-1}, SEM was performed on cryo-fractured samples, and TEM was performed on samples that had been cryo-microtomed and then stained with RuO_4.

Similarly, the behavior and morphology of **SEBS** were demonstrated to be independent of the presence of **BTA** assemblies in the melt. A comparison of the SAXS patterns of **PP/SEBS** and **PP/SEBS/BTA** at a given temperature (e.g., 100 °C or at room temperature) reveals no significant variation in the shape of the peak or in the value of $q_{L,max}$ (Figures 4A; S10, Supporting Information, respectively). In addition, the intensity evolution of the **SEBS** lamellae scattering peak for these two compositions are analogous upon cooling below the $T_{ODT,SEBS}$ (i.e., the first transition occurring upon cooling, Figure 4B,C). $T_{ODT,SEBS}$ in **PP/SEBS/BTA** was determined to be 166 °C, which is comparable to the value obtained in **PP/SEBS** (Figures S11 and S12, Supporting Information). Its organization into a comparable lamellar morphology upon cooling was also demonstrated by TEM imaging (Figures 3G; S13, Supporting Information) and POM by the appearance of Maltese crosses in the dispersed **SEBS** droplets (Figurea 3E; S8A,C, Supporting Information). It is important to note that the visualization of lamellae by TEM depends on the thickness of the sample being observed. The apparent variation in the definition of the lamellae across the different images presented in this work are attributed to differences in sample thickness rather than intrinsic structural variation.

2.3.2. Competitive Nucleation

The nucleation efficiency of a nucleating agent is directly related to the increase in the crystallization temperature of the semicrystalline matrix.[56] Given the orthogonal assembly of **BTA** and **SEBS** and the discrepancy of $T_{c,PP}$ in **PP/BTA** and **PP/SEBS** (126 and 130 °C, respectively), we predicted that the nucleation of **PP** would be dictated by the **SEBS** phase. Indeed, the DSC analysis (Figures S14 and S15, and Table S3, Supporting Information) suggests that the **SEBS** domains maintain their **PP** nucleation efficiency upon addition of **BTA**, as the peak $T_{c,PP}$ values in **PP/SEBS** and **PP/SEBS/BTA** were both found to be

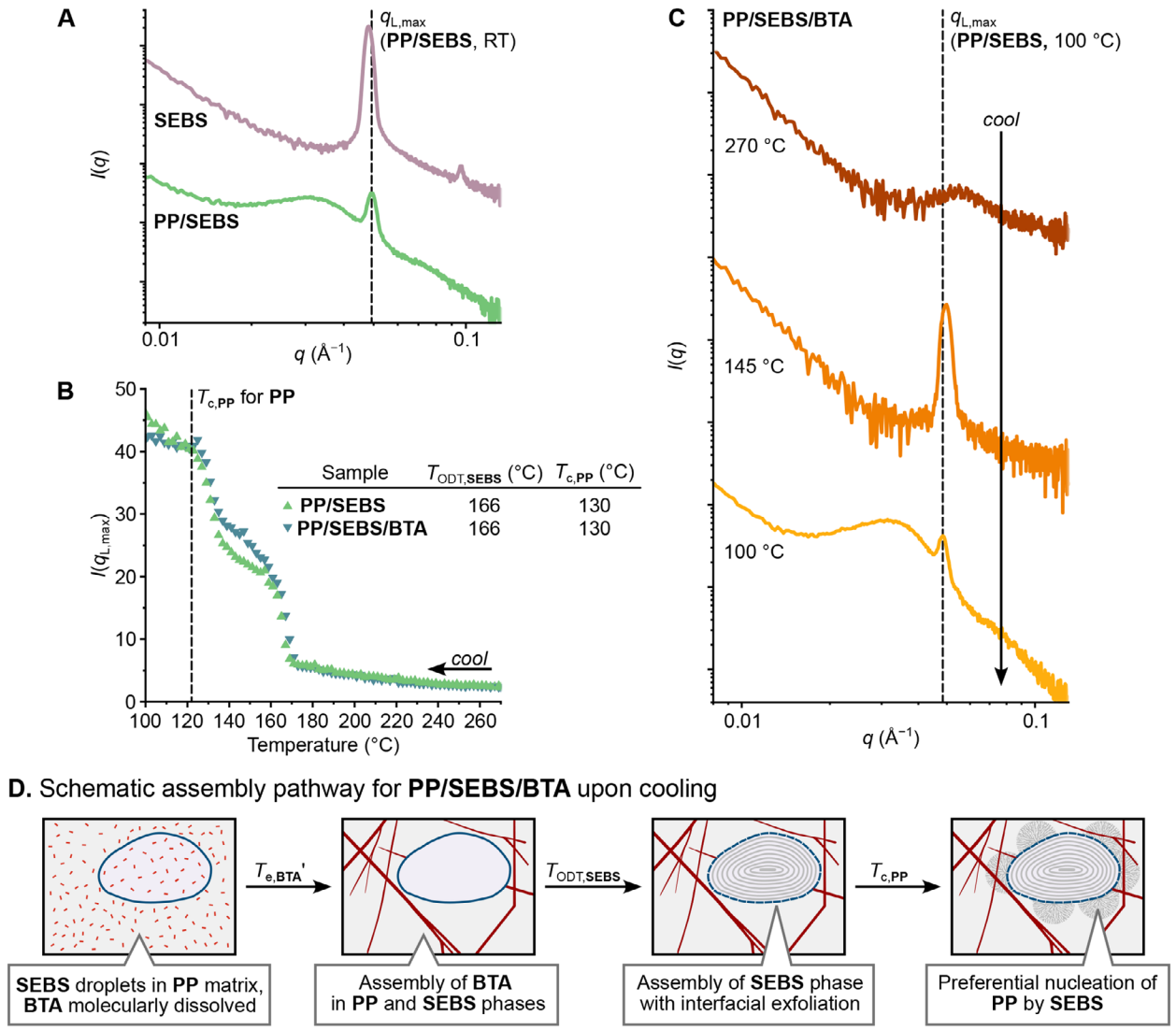

Figure 4. A) Room-temperature small-angle X-ray scattering (SAXS) patterns for **SEBS** and **PP/SEBS** after cooling at −1 °C min^{-1}. The dashed line indicates the scattering vector of the **SEBS** lamellae peak intensity ($q_{L,max}$) in **PP/SEBS** at room temperature. The plots were vertically shifted by two decades for clarity. B) Maximum of the SAXS signal intensity between 4.5 × 10^{-2} and 7.5 × 10^{-2} Å^{-1} for **PP/SEBS** and **PP/SEBS/BTA** upon cooling at −1 °C min^{-1}. The dashed line indicates the peak **PP** crystallization temperature ($T_{c,PP}$) measured for pristine **PP** by differential scanning calorimetry (DSC). C) Variable-temperature SAXS patterns for **PP/SEBS/BTA** at selected temperatures upon cooling at −1 °C min^{-1}. The plots were vertically shifted by three decades for clarity. The dashed line highlights $q_{L,max}$ in **PP/SEBS** at 100 °C. D) Schematic assembly pathway for **PP/SEBS/BTA** upon cooling.

130 °C. These results are in agreement with the SAXS measurements (Figures 4B; S11 and S12, Supporting Information). TEM revealed a similar interfacial exfoliated morphology of **SEBS** droplets in **PP/SEBS/BTA** to that observed in **PP/SEBS** (Figures 3G; S16, Supporting Information). Ultimately, the number of nuclei formed upon **PP** crystallization (hundreds of nuclei per 0.1 mm^2) and the diameter of the yielded spherulites (≈25 µm) were found by POM to be nearly identical in both compositions (Figure S8D,E, Supporting Information).

The competing assembly mechanisms in **PP/SEBS/BTA** as a function of temperature are schematically summarized in Figure 4D. At high temperature, **BTA** is dispersed throughout the material, and **SEBS** forms phase-separated droplets in the molten **PP**. Upon cooling, **BTA** forms large needle-like structures throughout the **PP** and **SEBS** phases. Further cooling causes the **SEBS** to organize into a lamellar structure with a distinct tendency to exfoliate at the **PP–SEBS** interface. The assembly of **BTA** and **SEBS** appears to be orthogonal; given the higher nucleating efficiency of **SEBS**, **PP** is nucleated by the rough texture at the **PP–SEBS** interface.

2.4. gSEBS Assembly in the Bulk and Coassembly with SEBS in PP/SEBS/gSEBS

The initial studies described above served to establish the orthogonality of **BTA** and **SEBS** assembly. They were also critical as a comparison for increasingly complex compositions containing

the compartmentalization agent **gSEBS**. Below, we first consider the bulk properties of **gSEBS** and its coassembly with **SEBS** in **PP** before establishing its ability to induce compartmentalization with **BTA**.

2.4.1. Bulk Properties of *gSEBS*

Analysis of bulk **gSEBS** by SAXS at room temperature revealed a lamellar morphology with a long period of 13.3 nm (Figure S17, Supporting Information), which is slightly larger than that observed for **SEBS** in the bulk (Figure S18, Supporting Information). This is likely a consequence of the bulky pendant **BTA** moieties interfering with the packing of the **SEBS** chains. The 33 °C decrease between $T_{ODT,SEBS}$ (166 °C, Figures S51 and S52, Supporting Information) and $T_{ODT,gSEBS}$ (133 °C, Figures S19 and S20, Supporting Information) measured in bulk via variable-temperature SAXS also suggest weaker or less interactions in this case.

2.4.2. Coassembly of *SEBS* and *gSEBS*

Variable-temperature FTIR study of **PP/SEBS/gSEBS** confirmed that the grafted BTAs are fully dissociated at processing temperatures and self-assemble through a nucleation-elongation process upon cooling (**Figures 5A**; S21, Supporting Information). The fitted $T_{e,BTA}$ for this composition (228 °C) is remarkably high considering the relatively low average BTA concentration (2.8 µmol g^{-1}), the nature of their substituents, and their expected solubility in the matrix (i.e., combination of PEB- and PS-based segments). This discrepancy can be attributed to the high local concentration in BTAs due to being grafted to the covalent polymer chain as well as their confinement in the **gSEBS**/**SEBS** domains. The cooling and heating curves display no hysteresis, which can be attributed to the reduction of the influence of monomer diffusion and a less cooperative assembly mechanism. No needle-like structures were discernible by POM (**Figures 6A**; S22B,C, Supporting Information), which may be ascribed to the steric hindrance induced by the polymeric substituent of the grafted BTAs, disfavoring lateral aggregation.

Blending **gSEBS** with **SEBS** had no significant effect on the block copolymer organization in **PP**. A similar $q_{L,max}$ was measured at room temperature for **PP/SEBS** and **PP/SEBS/gSEBS**, 4.93×10^{-2} and 4.91×10^{-2} $Å^{-1}$, respectively (Figure 5B). Also, $T_{ODT,SEBS}$ and $T_{ODT,gSEBS}$ were detected at the same temperature in both samples by variable-temperature SAXS (166 °C, Figures 5C; S23 and S24, Supporting Information). The lamellar organization of the triblock copolymers was also corroborated by the appearance of Maltese crosses by POM at 166 °C (Figures 6A; S22C, Supporting Information) and the regular lamellar organization visible by TEM (Figure S25, Supporting Information).

2.4.3. Nucleation of *PP* by Coassembled *SEBS/gSEBS*

Further analysis demonstrated that the dispersed **SEBS**/**gSEBS** droplets still acted as a nucleating agent for **PP**, but with decreased efficiency. A 5 °C decrease in $T_{c,PP}$ was measured between **PP/SEBS** and **PP/SEBS/gSEBS** by DSC (Figure S26 and Table S3, Supporting Information), and an equivalent decrease was estimated by variable-temperature SAXS (Figures 5C; S23 and S24, Supporting Information), giving a peak $T_{c,PP}$ only 3 °C above the one observed for pristine **PP**. This observation was corroborated by POM imaging, as it revealed a significant decline in the number of nuclei formed at the onset of crystallization, with only tens

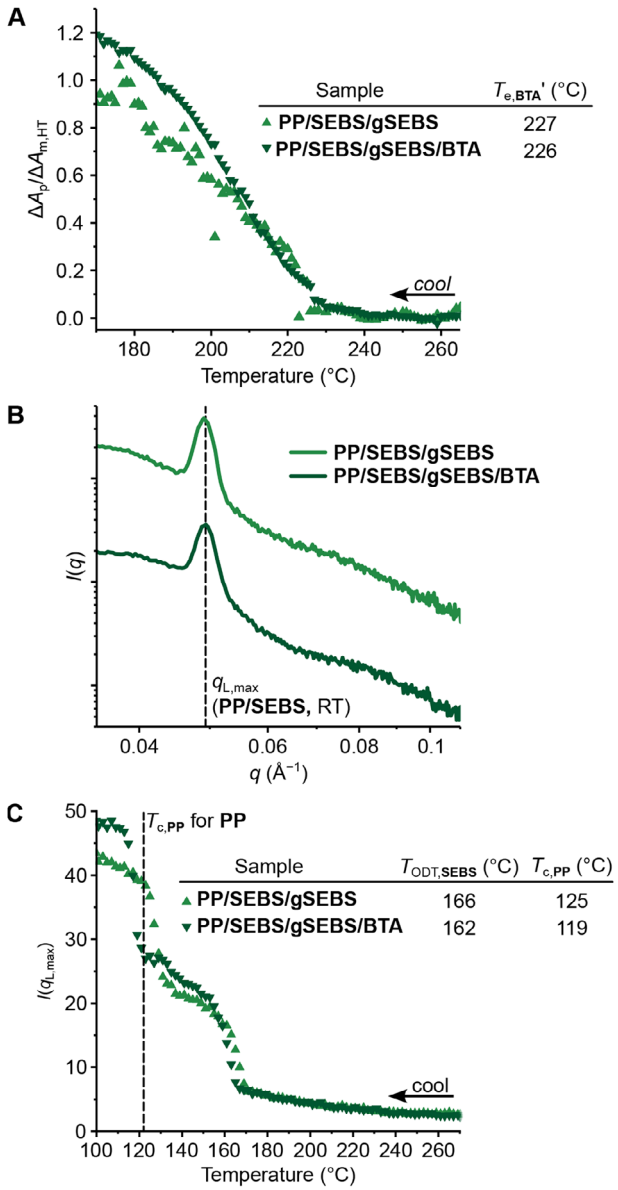

Figure 5. A) FTIR spectroscopy cooling curves of BTAs assembly in **PP/SEBS/gSEBS** and **PP/SEBS/gSEBS/BTA** at a rate of −1 °C min^{-1}. B) Room-temperature SAXS patterns for **PP/SEBS/gSEBS** and **PP/SEBS/gSEBS/BTA** after cooling at −1 °C min^{-1}. The plots were vertically shifted by one decade for clarity. The dashed line highlights $q_{L,max}$ in **PP/SEBS** at room temperature. C) Maximum SAXS signal intensity between 4.5×10^{-2} and 7.5×10^{-2} $Å^{-1}$ for **PP/SEBS/gSEBS** and **PP/SEBS/gSEBS/BTA**, respectively, upon cooling at −1 °C min^{-1}. The dashed line highlights the peak **PP** crystallization temperature ($T_{c,PP}$) measured in pristine **PP** by DSC.

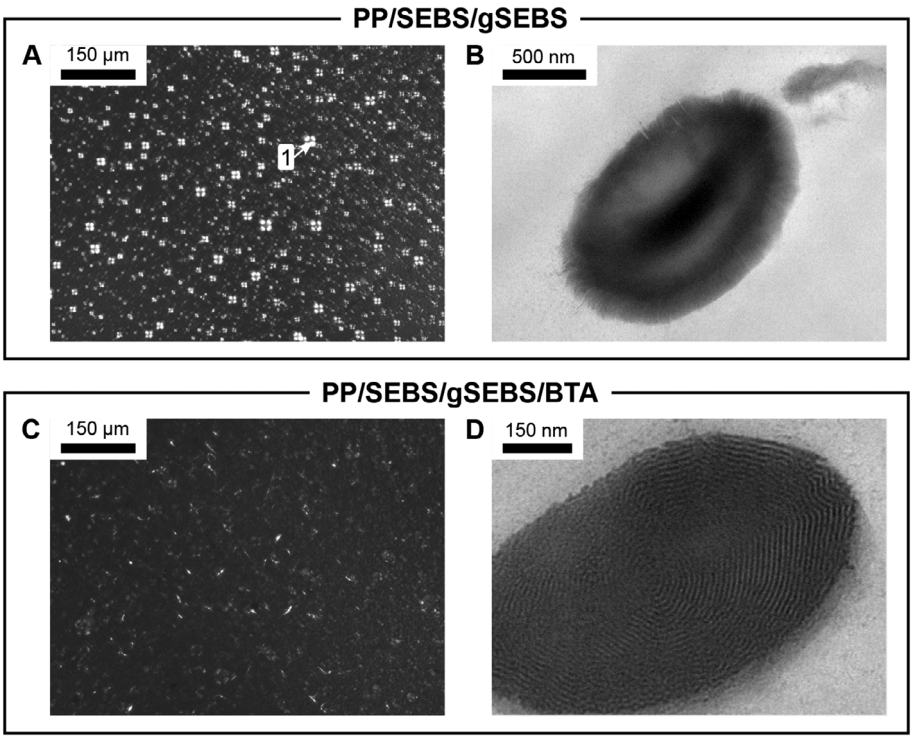

Figure 6. A) POM image of **PP/SEBS/gSEBS** at 145 °C. B) TEM image of **PP/SEBS/gSEBS**. C) POM image of **PP/SEBS/gSEBS/BTA** at 162 °C. D) TEM image of **PP/SEBS/gSEBS/BTA**. Label 1 corresponds to the **SEBS/gSEBS** domains. POM images were acquired while cooling at −1 °C min^{-1} and TEM was performed on samples that had been cryo-microtomed and then stained with RuO_4.

of nuclei formed per 0.1 mm^2 for **PP/SEBS/gSEBS**, resulting in an increase in the average spherulite size (Figure S22D,E, Supporting Information).

The diminished nucleating performance of **PP/SEBS/gSEBS** was traced to a change in the surface texture of the **SEBS/gSEBS** droplets. The TEM study of **PP/SEBS/gSEBS** qualitatively indicated a reduction in the degree of exfoliation of the lamellae compared to **PP/SEBS**, as the **PP** intercalation within the triblock lamellae manifests to a lesser extent, thus leaving fewer nucleation sites (Figures 6B; S25, Supporting Information). SEM observations also revealed scarce fiber-like features at interfaces in **PP/SEBS/gSEBS**, especially after the selective dissolution of the **SEBS/gSEBS** phase (Figures S27 and S28, Supporting Information). We hypothesized that the introduction of the polar BTA moieties in the PEB domains reduced its compatibility with **PP**, leading to less interpenetration, less exfoliation, and thus a smoother interface. Furthermore, the incorporated BTA units were unable to induce nucleation of the **PP** matrix, as their assembly was limited to forming small objects confined to the **SEBS/gSEBS** domains.

2.5. Compartmentalization Induced by gSEBS in PP/SEBS/gSEBS/BTA

*2.5.1. Orchestrating the Assembly of **SEBS** and **BTA** with **gSEBS***

Comprehensive analysis of **PP/SEBS/gSEBS/BTA** demonstrated that **gSEBS** was a powerful compartmentalization agent capable of coassembling both with the non-grafted **BTA** and the non-grafted block copolymer **SEBS**. The comparison of the FTIR spectroscopy heating and cooling curves of **PP/SEBS/BTA** and **PP/SEBS/gSEBS/BTA** demonstrates that introducing **gSEBS** leads to a decrease in the cooperativity of **BTA** assembly (Figures 5A; S29, and Table S2, Supporting Information). Moreover, the undercooling (i.e., $\Delta T = T_{e,BTA} - T_{e',BTA}$) goes from 8 to 0 °C in the absence (Figure 2B,C) and the presence (Figures 5A; S29, and Table S2, Supporting Information) of **gSEBS**, respectively. The evolution of the shape of these curves provides compelling evidence of non-orthogonality between **gSEBS** and **BTA**, particularly because less cooperative processes are expected from coassembly with bulky aggregators such as **gSEBS**.[57,58]

Analysis of **PP/SEBS/gSEBS/BTA** by SAXS confirmed that **SEBS** and **gSEBS** chains co-organize in a lamellar morphology in the presence of **BTA** based on the distinctive scattering peak at a $q_{L,max}$ of 4.92×10^{-2} $Å^{-1}$ at room temperature (Figures 5B; S30, Supporting Information), which is essentially the same as that observed for **PP/SEBS/gSEBS**. The lamellar organization of the block copolymers in the dispersed phase was once again supported by direct observation via TEM (Figure S31, Supporting Information). The T_{ODT} was measured by variable-temperature SAXS to be 162 °C, which corresponds to a moderate 4 °C decrease compared to **PP/SEBS** and **PP/SEBS/gSEBS** (Figures 5C; S32 and S33, Supporting Information). This discrepancy could be explained by the loss of chain mobility induced by BTA aggregation.

As a comparison, we analyzed a sample of **SEBS/gSEBS/BTA** (i.e., no **PP** matrix) at room-temperature by SAXS after cooling

it from the melt at −1 °C min^{-1}. This composition approximates the behavior of a fully **BTA**-loaded dispersed phase (Table S1, Supporting Information). This sample exhibited a comparable lamellar morphology to that observed in **PP/SEBS/gSEBS/BTA** (Figure S30, Supporting Information), further confirming that the formation of BTA fibers in the **SEBS/gSEBS** phase does not perturb the periodic dimensions of the lamellae.

2.5.2. Consequences of Compartmentalization on Nucleating Properties, Melt Viscoelasticity, and Morphology

The introduction of **gSEBS** induced a strong reduction of the nucleating properties of the additives. The peak $T_{c,PP}$ in **PP/SEBS/gSEBS/BTA** of 119 °C measured by DSC (Figure S34 and Table S3, Supporting Information) and SAXS (Figures 5C; S32 and S33, Supporting Information) was 3 °C *lower* than for pristine, non-nucleated **PP**. Also, $T_{c,PP}$ for **PP/SEBS/gSEBS/BTA** was 6 °C less than that of **PP/SEBS/gSEBS**, which provocatively suggests that the addition of **BTA** shut down the nucleating properties of this ensemble of additives. POM observations of **PP/SEBS/gSEBS/BTA** (Figure S35D,E, Supporting Information) were consistent with those of non-nucleated **PP** (Figure S49, Supporting Information) with only a few nuclei formed per 0.1 mm^2, resulting in the formation of large spherulites that exceeded 500 µm in diameter.

This behavior was rationalized by the discovery that **gSEBS** induced the compartmentalization of **BTA** assemblies within the **SEBS/gSEBS** domains. POM revealed minimal birefringence within the typical temperature range of BTA assembly (Figures 6C; S35, Supporting Information). Careful examination of the morphology of **PP/SEBS/gSEBS/BTA** by SEM (Figures S36 and S37, Supporting Information) and TEM (Figures 6D; S31, Supporting Information) revealed no evidence of 1D structures attributable to BTA assemblies in **PP**.

This conclusion was further substantiated by startup flow experiments conducted on blends at 150 °C (Supporting Information). These experiments were performed at a rate such that all **BTA**-free compositions were tested close to linear viscoelastic regime, as evidenced by the similar monotonic or slightly non-monotonic behavior (**Figures** 7A; S38, Supporting Information). Comparing **PP/SEBS** to **PP/SEBS/BTA**, the addition of **BTA** produces a substantial stress overshoot attributable to the disruption and orientation of **BTA** aggregates within the polymer matrix. This same feature was distinctly observed in **PP/PS/BTA** and **PP/SEBS/BTA,** but it was absent in the case of both **PP/SEBS/gSEBS** and **PP/SEBS/gSEBS/BTA** (Figure S38, Supporting Information). The singular response exhibited by **PP/SEBS/gSEBS/BTA** in comparison to the other **BTA**-containing blends validates the absence of a BTA supramolecular network in the **PP** continuous phase.

Compartmentalization of the **BTA** fibers in **PP/SEBS/gSEBS/BTA** was further substantiated through the use of energy-dispersive X-ray spectroscopy (EDS) coupled to TEM by semi-quantitatively monitoring the nitrogen content in specific regions of interest (Figures 7B; S39–S41, and Table S4, Supporting Information). Every analysis conducted within the **PP** background yielded a null nitrogen content, while the global concentration in BTAs in the dispersed phase in **PP/SEBS/gSEBS/BTA** (average nitrogen content of 9.9 wt.%) is substantially higher than in **PP/SEBS/gSEBS** (average nitrogen content of 4.3 wt.%), and no nitrogen could be detected in **PP/SEBS**. This outcome is consistent with the evolution in the amount of added **BTA** and its complete partitioning to the **SEBS/gSEBS** domains in **PP/SEBS/gSEBS/BTA**.

Ultimately, atomic force microscopy (AFM) allowed for the direct detection of the BTA fibers in **PP/SEBS/gSEBS/BTA**, confirming their compartmentalization in the block copolymer phase (Figures 7C; S42 and S43, Supporting Information). The size and high energy dissipation of block copolymer droplets, in conjunction with the presence of lamellar structures, rendered them readily distinguishable from the **PP** matrix. The observation of **PP/SEBS/gSEBS/BTA** revealed the presence of numerous short and thin fibrillar features restricted to the dispersed phase, which did not appear in **PP/SEBS/BTA** and which can be ascribed to **BTA** assemblies. The formation of shorter fibers is in accordance with the decrease in cooperativity observed in the heating and cooling curves by FTIR spectroscopy (Figure 5A), which implies a decrease in the average degree of polymerization.[59] Furthermore, the bulkiness of the polymeric substituent of the grafted BTA units impedes lateral organization of the BTA fibers, resulting in the formation of thinner supramolecular structures.

The compartmentalization of **BTA** within the **SEBS/gSEBS** domains had a surprisingly pronounced impact on the surface morphology of this phase. As evidenced by TEM (Figures 6D; S31, Supporting Information) and SEM (Figures S36 and S37, Supporting Information), the **SEBS/gSEBS** domains displayed a smooth surface; the interfacial exfoliation of the lamellae by **PP** was strongly suppressed. The nucleating efficiency of the **SEBS/gSEBS** phase was thus shut down. It is noteworthy that the signal corresponding to Maltese crosses by POM, which is associated with a lamellar morphology, is significantly weaker, and, in some cases, even absent for many droplets (Figure 6C). However, room-temperature SAXS measurements (Figure 5B) and TEM imaging (Figure 6D) unambiguously indicate a lamellar organization of the triblock copolymers. This apparent discrepancy is explained by the organization of the triblock copolymer in the same morphology but in smaller domain sizes (Figures 6D; S31, Supporting Information), which can lead to diminished birefringence.

As the self-organization of block copolymers is also a nucleation-growth process,[60–62] the reduction in lamellae domain size could be attributed to the decrease in cooperativity of **SEBS** assembly induced by coassembly with **gSEBS** and the consequential partitioning of **BTA** to the block copolymer phase. Another important factor is that the assembly of the **BTA** led to a reduction in the compatibility of **PP** with the PEB lamellae when compared to **PP/SEBS/gSEBS** and **PP/SEBS**. This enhanced incompatibility could reduce the thermodynamic favorability of **PP** to mix with the PEB phase, thus suppressing exfoliation of the lamellae.

2.5.3. Rationalization and Discussion of Compartmentalization

The compartmentalization was attributed to the presence of weak interactions, well above $T_{e,BTA}$, between **BTA** and the pendant moieties of **gSEBS**, which acts as a surfactant and thereby

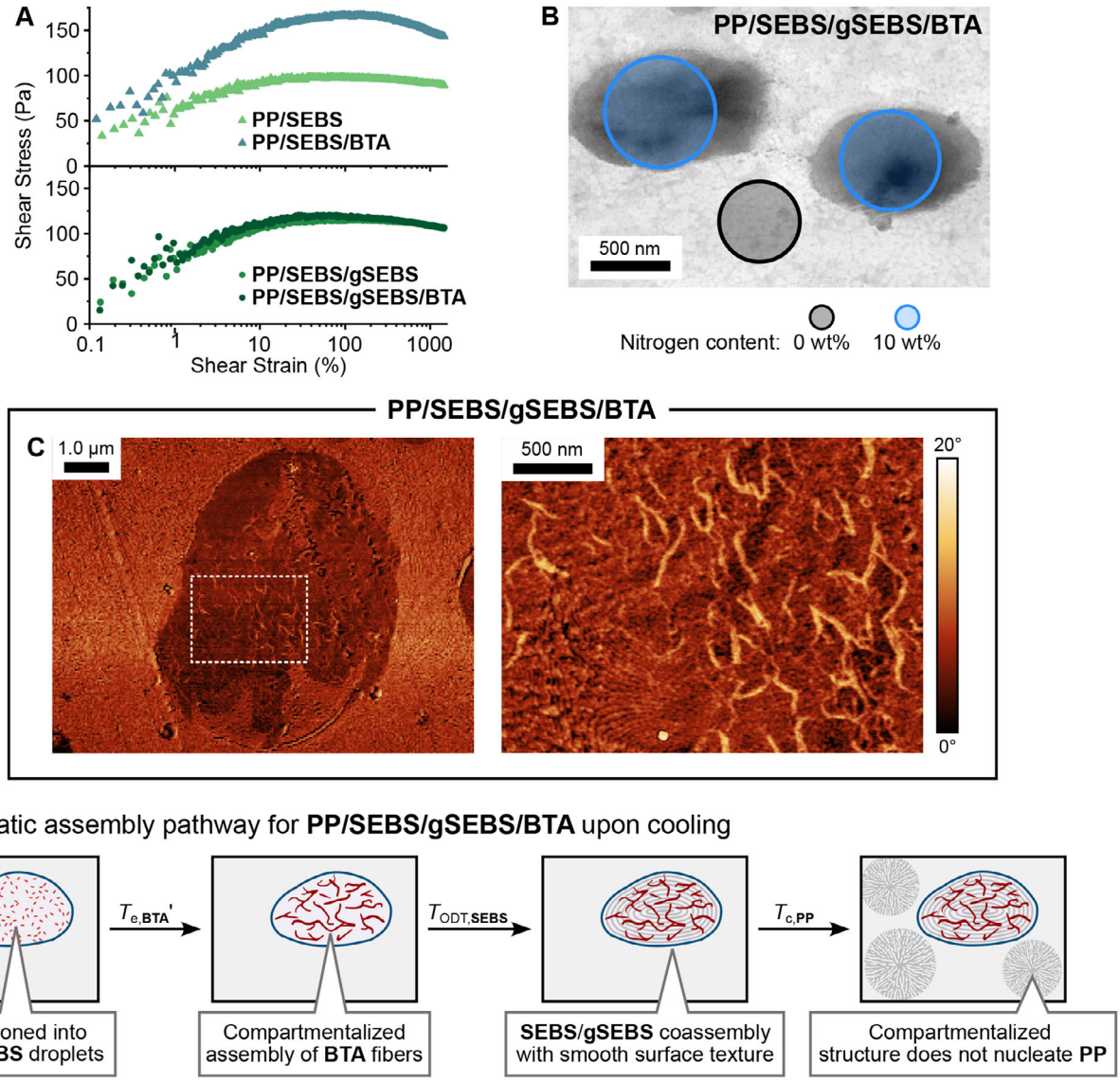

Figure 7. A) Startup flow experiments (shear rate = 0.05 s^{-1}) for **PP/SEBS** and **PP/SEBS/BTA** (top) and for **PP/SEBS/gSEBS** and **PP/SEBS/gSEBS/BTA** (bottom). B) TEM image of **PP/SEBS/gSEBS/BTA** after RuO_4 staining, coupled with energy-dispersive X-ray spectroscopy (EDS) analysis. Areas of EDS analysis are circled and colored depending on the resulting nitrogen content. C) Phase atomic force microscopy (AFM) images of **PP/SEBS/gSEBS/BTA**. D) Schematic assembly pathway for **PP/SEBS/gSEBS/BTA** upon cooling.

specifically stabilizes the **BTA** dispersion to the block copolymer phase. In a related system, weakly hydrogen-bonded states were observed at elevated temperatures by FTIR spectroscopy in the study of BTA dispersion in the presence of a BTA-end-functionalized polymer matrix.[37,63] This hypothesis was thus supported by the singular presence of an additional broad absorption band (3435–3450 cm^{-1}) within the N—H stretching region of the FTIR spectra of **PP/SEBS/gSEBS/BTA** above $T_{e,BTA}$ (e.g., at 260 °C, Figure S55, Supporting Information). This signal, which is indicative of weakly hydrogen-bonded amides, is slightly shifted toward lower wavenumbers compared to the monomeric **BTA** band (3440–3480 cm^{-1}). The absence of this feature in **PP/PS/BTA** and **PP/SEBS/BTA** FTIR spectra at analogous temperatures further corroborates the distinct role of **gSEBS** in this phenomenon. The fact that the $T_{c,PP}$ of **PP/SEBS/gSEBS/BTA** is 4 °C lower than that of **PP** is likely explained by a proportion of polar heterogeneities being partitioned[17] to the **SEBS/gSEBS** phase along with **BTA**.

All of the insights into the hierarchical structure of **PP/SEBS/gSEBS/BTA** as a function of temperature are graphically summarized in Figure 7D; it is useful to compare with the simpler organization of **PP/SEBS/BTA** in Figure 4D. At high temperature, **SEBS** and **gSEBS** form droplets in the molten **PP** matrix, and **BTA** is partitioned to this **SEBS/gSEBS** phase because of the compatibilizing effect of **gSEBS**. Upon cooling, **BTA** assembles into thin fibers within the **SEBS/gSEBS** phase, and further cooling leads to the organization of **SEBS/gSEBS** into a lamellar structure with a relatively smooth interface with

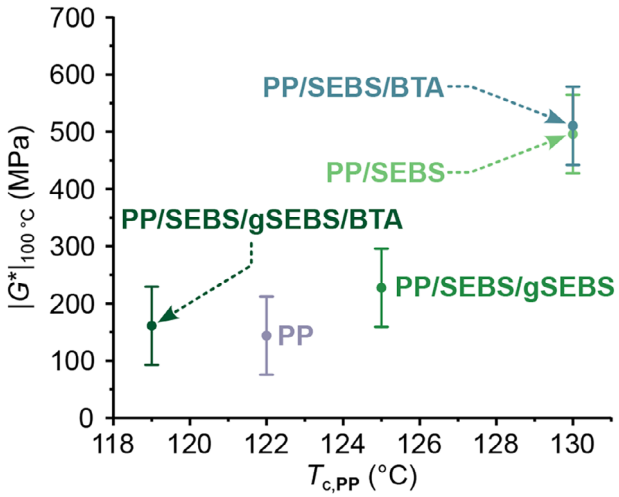

Figure 8. Plot of the absolute value of the complex shear modulus at 100 °C ($|G^*|_{100\,°C}$, fitted from amplitude sweep measurements in the linear regime at an oscillation frequency of 1 Hz) versus the **PP** peak crystallization temperature ($T_{c,PP}$, measured by DSC) for the compositions of interest. The bars represent the measurements standard deviation.

the **PP** matrix. The compartmentalization of the **BTA** to the **SEBS/gSEBS** phase resulted in a complete suppression of the nucleating properties of these additives, and thus, **PP** formed large spherulites that were presumably nucleated by some remaining heterogeneities throughout the material.

2.5.4. Consequences of Compartmentalization on Thermomechanical Properties

We sought to characterize how the formulation of these blends influences the thermomechanical properties of the material. Due to the practical constraints associated with conducting tensile tests on samples with finely controlled thermal history, a rheological study with a cone-plate geometry was selected as an alternative method. Oscillatory shear amplitude sweep measurements in the linear regime in the solid state at 100 °C enabled the determination of shear stiffness, as they can yield the absolute value of the complex shear modulus, $|G^*|_{100\,°C}$.

These experiments revealed a clear positive correlation between $T_{c,PP}$ and $|G^*|_{100\,°C}$, indicating that compositions presenting higher nucleation efficiency exhibited increased stiffness (**Figure 8**). This relationship has been previously reported and was attributed, in particular, to the increase in average **PP** lamellar thickness with crystallization temperature, which leads to an increase in stiffness.[64–66] These findings underscore the significance of the hierarchical organization of composition in determining mechanical properties at the macroscale. In turn, the assembly of the system, which occurs over many length scales, has been deeply tuned by controlling the formulation and the multimolecular interactions.

3. Conclusion

In conclusion, we have exemplified the compartmentalization of the nucleating agents **BTA** and **SEBS** within the semicrystalline polyolefin matrix **PP**. Based on a systematic study, **BTA** and **SEBS** orthogonally self-assemble and nucleate the **PP** matrix according to their competitive nucleating efficiency. Compartmentalization was induced by adding **gSEBS**, a functional copolymer capable of coassembling with both **BTA** and **SEBS**. The introduction of **gSEBS** caused **BTA** to segregate to the **SEBS** domains at high temperature, which caused **BTA** fibers to exclusively form in this phase. Although the assembly of **BTA** did not perturb the nanoscale lamellar organization of the **SEBS** phase, it suppressed the exfoliation of the lamellae by **PP** at the **SEBS–PP** interface. The combination of these two features—the segregation of the **BTA** fibers and the alteration of the **SEBS–PP** interface—resulted in the complete loss of nucleating properties of these additives. The thermomechanical properties of the compartmentalized material were essentially the same as those of the virgin **PP**, confirming the successful compartmentalization of **BTA** and **SEBS**.

We believe that this work represents a remarkable counterpoint to previous examples of compartmentalization in semicrystalline materials. Instead of releasing a functional chemical cargo from domains distributed throughout a matrix, allowing the cargo to perform a specific function, we have demonstrated the recruitment of functional additives into a dispersed phase, thereby suppressing their activity. We believe that this concept is promising for applications that demand the spatial control of polymer additives. Future work will be dedicated to structure-property relationships that govern compartmentalization, kinetic effects, and exemplification of practical applications.

Supporting Information

Supporting Information is available from the Wiley Online Library or from the author.

Acknowledgements

Financial support from the Agence Nationale de la Recherche (ANR) is gratefully acknowledged (ANCHORS project, ANR-21-CE06-0008). The authors thank the FCMat (Fédération de Chimie et Matériaux Paris Centre-FR2482) and the C'Nano projects of the Région Ile-de-France for the TEM and X-ray scattering measurements. Nippon Soda Company is gratefully acknowledged for supplying the SBS. The authors wish to thank Alexi Riba-Bremerch (ESPCI), Gaëlle Carré De Lusancay (ESPCI), and Mickaël Pomes-Hadda (ESPCI) for technical support. The authors also wish to thank Beatrice Adelizzi (Danone), James Eagan (U. Akron), Renaud Nicolaÿ (ESPCI), François Tournilhac (ESPCI), Holger Frauenrath (EPFL), and Bert Meijer (TU/e) for stimulating discussions.

Conflict of Interest

The authors declare no conflict of interest.

Data Availability Statement

The data that support the findings of this study are available in the supplementary material of this article.

Keywords

block copolymers, coassembly, crystallization, nucleation, supramolecular chemistry

Received: June 30, 2025
Revised: August 21, 2025
Published online:

[1] I. S. Choi, N. Bowden, G. M. Whitesides, *Angew. Chem., Int. Ed.* **1999**, *38*, 3078.
[2] A. H. Chen, P. A. Silver, *Trends Cell Biol.* **2012**, *22*, 662.
[3] C. A. Kerfeld, C. Aussignargues, J. Zarzycki, F. Cai, M. Sutter, *Nat. Rev. Microbiol.* **2018**, *16*, 277.
[4] L. Schoonen, J. C. van Hest, *Adv. Mater.* **2016**, *28*, 1109.
[5] O. J. G. M. Goor, S. I. S. Hendrikse, P. Y. W. Dankers, E. W. Meijer, *Chem. Soc. Rev.* **2017**, *46*, 6621.
[6] T. Trantidou, M. Friddin, Y. Elani, N. J. Brooks, R. V. Law, J. M. Seddon, O. Ces, *ACS Nano* **2017**, *11*, 6549.
[7] T. Pelras, C. S. Mahon, M. Mullner, *Angew. Chem., Int. Ed.* **2018**, *57*, 6982.
[8] D. Bracha, M. T. Walls, C. P. Brangwynne, *Nat. Biotechnol.* **2019**, *37*, 1435.
[9] J. Huang, Y. Guo, S. Gu, G. Han, W. Duan, C. Gao, W. Zhang, *Polym. Chem.* **2019**, *10*, 3426.
[10] C. G. Palivan, L. Heuberger, J. Gaitzsch, B. Voit, D. Appelhans, B. Borges Fernandes, G. Battaglia, J. Du, L. Abdelmohsen, J. C. M. van Hest, J. Hu, S. Liu, Z. Zhong, H. Sun, A. Mutschler, S. Lecommandoux, *Biomacromolecules* **2024**, *25*, 5454.
[11] R. Harris, N. Berman, A. Lampel, *Chem. Soc. Rev.* **2025**, *54*, 4183.
[12] S. J. Barrow, S. Kasera, M. J. Rowland, J. del Barrio, O. A. Scherman, *Chem. Rev.* **2015**, *115*, 12320.
[13] C. Calvino, C. Weder, *Small* **2018**, *14*, 1802489.
[14] B. Jiang, M. Mu, Y. Zhou, J. Zhang, W. Li, *Small* **2024**, *20*, 2311897.
[15] Y. Wu, M. Tang, M. L. Barsoum, Z. Chen, F. Huang, *Chem. Soc. Rev.* **2025**, *54*, 2906.
[16] Plastics Europe, The Circular Economy for Plastics – A European Analysis 2024, https://plasticseurope.org/knowledge-hub/the-circular-economy-for-plastics-a-european-analysis-2024/ (accessed: February 2025).
[17] S. E. Fenni, A. J. Müller, D. Cavallo, *Polymer* **2023**, *264*, 125514.
[18] R. M. Michell, A. J. Müller, *Prog. Polym. Sci.* **2016**, *54–55*, 183.
[19] E. Carmeli, S. E. Fenni, M. R. Caputo, A. J. Müller, D. Tranchida, D. Cavallo, *Macromolecules* **2021**, *54*, 9100.
[20] W. Wang, S. Buzzi, S. E. Fenni, E. Carmeli, B. Wang, G. Liu, A. J. Müller, D. Cavallo, *Macromol. Chem. Phys.* **2022**, *223*, 2200202.
[21] *Handbook of Polymer Crystallization* (Eds: E. Piorkowska, G. C. Rutledge), Wiley, Hoboken, New Jersey **2013**.
[22] G. Wypych, *Handbook of Nucleating Agents*, ChemTec Publishing, Ontario, Canada **2016**.
[23] B. Lotz, T. Miyoshi, S. Z. D. Cheng, *Macromolecules* **2017**, *50*, 5995.
[24] S. Shi, W. Liu, M. Nie, Q. Wang, *RSC Adv.* **2016**, *6*, 98104.
[25] S. Shi, P. Huang, M. Nie, Q. Wang, *Polymer* **2017**, *132*, 23.
[26] S. Shi, Y. Liu, M. Nie, Q. Wang, *Ind. Eng. Chem. Res.* **2019**, *58*, 4116.
[27] K. Zhang, R. Han, M. Nie, Q. Wang, *Ind. Eng. Chem. Res.* **2019**, *58*, 22283.
[28] Y. Zhang, G. Luo, Y. Niu, G. Li, *Polymer* **2023**, *264*, 125539.
[29] W.-y. Zhuo, J. Wang, Y.-h. Niu, Y.-d. Lv, *Polymer* **2025**, *316*, 127893.
[30] Z. O. G. Schyns, M. P. Shaver, *Macromol. Rapid Commun.* **2021**, *42*, 2000415.
[31] X. Gao, J. Guo, D. Zhang, J. Li, Y. Su, F. Arbeiter, H. Li, *J. Polym. Sci.* **2024**, *62*, 3025.
[32] G. J. M. Formon, J. Jayaratnam, C. Guibert, N. J. Van Zee, R. Nicolaÿ, *Macromolecules* **2024**, *57*, 8277.
[33] A. Quinteros-Sedano, B. Bresson, N. J. Van Zee, R. Nicolaÿ, *ACS Mater. Lett.* **2024**, *6*, 877.
[34] J. J. B. van der Tol, S. Hafeez, A. P. G. Banziger, H. Su, J. P. A. Heuts, E. W. Meijer, G. Vantomme, *Adv. Mater.* **2024**, *36*, 2410723.
[35] C. Y. Shi, W. Y. Qin, D. H. Qu, *Chem. Sci.* **2024**, *15*, 8295.
[36] D. Gorl, S. Haraguchi, Y. Hryshunin, S. Thiele, G. Scetta, A. Simula, M. Wendling, O. Oguz, N. Candau, T. Tanzer, M. Liebi, C. J. G. Plummer, H. Frauenrath, *Nat. Commun.* **2025**, *16*, 217.
[37] S. Thiele, M. Giffin, M. Wendling, D. Gorl, C. J. G. Plummer, H. Frauenrath, *Org. Chem. Front.* **2025**.
[38] A. Thierry, C. Straupé, J. C. Wittmann, B. Lotz, *Macromol. Symp.* **2006**, *241*, 103.
[39] C. De Rosa, M. Scoti, R. Di Girolamo, O. R. Ballesteros, F. Auriemma, A. Malafronte, *Polym. Cryst.* **2020**, *3*, 10101.
[40] H.-W. Schmidt, P. Smith, M. Blomenhofer, Ciba Specialty Chemicals Holding Inc, Basel, Switzerland *WO 02/46300 A2*, **2002**.
[41] D. Mäder, K. Hoffmann, H.-W. Schmidt, Ciba Specialty Chemicals Holding Inc, Basel, Switzerland *WO 03/102069 A1*, **2003**.
[42] M. Blomenhofer, S. Ganzleben, D. Hanft, H.-W. Schmidt, M. Kristiansen, P. Smith, K. Stoll, D. Mäder, K. Hoffmann, *Macromolecules* **2005**, *38*, 3688.
[43] P. M. Kristiansen, A. Gress, P. Smith, D. Hanft, H.-W. Schmidt, *Polymer* **2006**, *47*, 249.
[44] M. Kristiansen, P. Smith, H. Chanzy, C. Baerlocher, V. Gramlich, L. McCusker, T. Weber, P. Pattison, M. Blomenhofer, H.-W. Schmidt, *Cryst. Growth Des.* **2009**, *9*, 2556.
[45] M. W. Matsen, R. B. Thompson, *J. Chem. Phys.* **1999**, *111*, 7139.
[46] L. Leibler, *Macromolecules* **2002**, *13*, 1602.
[47] F. O. M. S. Abreu, M. M. C. Forte, S. A. Liberman, *J. Appl. Polym. Sci.* **2005**, *95*, 254.
[48] N. Fanegas, M. A. Gómez, C. Marco, I. Jiménez, G. Ellis, *Polymer* **2007**, *48*, 5324.
[49] A. Riba-Bremerch, *Coassembly of Nucleating Agents in Polymeric Media*, *PhD thesis*, Université PSL, Paris, France **2023**.
[50] A. Riba-Bremerch, A. Y. G. Delplanque, C. Guibert, N. J. Van Zee, *Chem. Sci.* **2025**, https://doi.org/10.1039/d5sc02678d.
[51] P. A. Weimann, T. D. Jones, M. A. Hillmyer, F. S. Bates, J. D. Londono, Y. Melnichenko, G. D. Wignall, K. Almdal, *Macromolecules* **1997**, *30*, 3650.
[52] S. B. Chun, C. D. Han, *Macromolecules* **1999**, *32*, 4030.
[53] D. Zhao, J. S. Moore, *Org. Biomol. Chem.* **2003**, *1*, 3471.
[54] H. M. ten Eikelder, A. J. Markvoort, T. F. de Greef, P. A. Hilbers, *J. Phys. Chem. B* **2012**, *116*, 5291.
[55] J. K. Kim, C. D. Han, in *Polymer Materials*, Vol. *231* (Eds.: K.-S. Lee, S. Kobayashi), Springer, Berlin, Heidelberg **2009**.
[56] B. Fillon, B. Lotz, A. Thierry, J. C. Wittmann, *J. Polym. Sci., Part B: Polym. Phys.* **1993**, *31*, 1395.
[57] C. Kulkarni, E. W. Meijer, A. R. A. Palmans, *Acc. Chem. Res.* **2017**, *50*, 1928.
[58] M. A. J. Veld, D. Haveman, A. R. A. Palmans, E. W. Meijer, *Soft Matter* **2011**, *7*, 524.
[59] T. F. De Greef, M. M. Smulders, M. Wolffs, A. P. Schenning, R. P. Sijbesma, E. W. Meijer, *Chem. Rev.* **2009**, *109*, 5687.
[60] N. P. Balsara, B. A. Garetz, M. Y. Chang, H. J. Dai, M. C. Newstein, J. L. Goveas, R. Krishnamoorti, S. Rai, *Macromolecules* **1998**, *31*, 5309.
[61] B. Stuehn, A. Vilesov, H. G. Zachmann, *Macromolecules* **1994**, *27*, 3560.
[62] G. Floudas, T. Pakula, E. W. Fischer, N. Hadjichristidis, S. Pispas, *Acta Polym.* **1994**, *45*, 176.
[63] A. Timme, R. Kress, R. Q. Albuquerque, H.-W. Schmidt, *Chem.-Eur. J.* **2012**, *18*, 8329.
[64] B. Pukánszky, I. Mudra, P. Staniek, *J. Vinyl Addit. Technol.* **1997**, *3*, 53.
[65] A. Menyhard, P. Suba, Z. Laszlo, H. M. Fekete, A. O. Mester, Z. Horvath, G. Voros, J. Varga, J. Moczo, *eXPRESS Polym. Lett.* **2015**, *9*, 308.
[66] *Polypropylene Handbook. Morphology, Blends and Composites*, (Eds: J. Karger-Kocsis, T. Bárány), Springer, Cham, Switzerland **2019**.